

# Characterization of absorption and non-linear effects in infrasound propagation using an augmented Burgers' equation

R. Sabatini,<sup>1,2</sup> C. Bailly,<sup>1</sup> O. Marsden<sup>1,3</sup> and O. Gainville<sup>2</sup>

<sup>1</sup>Laboratoire de Mécanique des Fluides et d'Acoustique, UMR CNRS 5509, École Centrale de Lyon, F-69134 Écully cedex, France.

E-mail: roberto.sabatini@doctorant.ec-lyon.fr

<sup>2</sup>CEA, DAM, DIF, F-91297, Arpaçon, France

<sup>3</sup>European Centre for Medium-Range Weather Forecasts (ECMWF), Shinfield Park, RG2 9AX Reading, United Kingdom

Accepted 2016 September 16. Received 2016 September 14; in original form 2016 May 4

## SUMMARY

The long-range atmospheric propagation of explosion-like waves of frequency in the infrasound range is investigated using non-linear ray theory. Simulations are performed for sources of increasing amplitude on rays up to the lower thermosphere and for distances of hundreds of kilometres. A study of the attenuation of the waveforms observed at ground level induced by both the classical mechanisms and the vibrational relaxation of the molecules comprising the atmospheric gas is carried out. The relative importance of classical absorption and vibrational relaxation along the typical atmospheric propagation trajectories is assessed. Non-linear effects are highlighted as well and particular emphasis is placed on their strong interaction with absorption phenomena. A detailed description of the propagation model and of the numerical algorithm used in this work is first reported. Results are then discussed and the importance of the different mechanisms is clarified.

**Key words:** Seismic monitoring and test-ban treaty verification; Guided waves; Wave propagation; Acoustic properties.

## 1 INTRODUCTION

Explosive sources generate low-frequency acoustic waves below a few Hertz that can be measured at very large distances (Campus & Christie 2010). The signal detected by barometric stations located at ground level consists of phases which propagate along particular paths through the atmospheric thermal layers and can reach altitudes up to the lower thermosphere. As a general rule, tropospheric, stratospheric and thermospheric arrivals are observed (Ottemöller & Evers 2007; Gainville *et al.* 2010; Fee *et al.* 2013).

Atmospheric absorption plays a major role in long-range propagation (Sutherland & Bass 2004). Along with the classical mechanisms associated with the viscous diffusion, the thermal conduction and the rotational modes of the molecules comprising the atmospheric gas (Pierce 1985), vibrational relaxation is a potential source of wave attenuation. Due to the vertical variability of the atmosphere, the influence of these phenomena on the recorded waveforms is related not only to the frequency of the wave, but also to the particular trajectory followed by the signal before reaching the ground (de Groot-Hedlin 2008). Roughly speaking, in the infrasound range, vibrational relaxation is expected to be more important for stratospheric or tropospheric arrivals. On the other hand, as a consequence of the approximately exponential reduction with height of the mean density, classical phenomena are the dominant absorption mechanisms along thermospheric phases. Together with

signal attenuation, non-linearity can be important for large source amplitudes and increases with decreasing density. Non-linear effects induce waveform distortion and modify the spectral content of the signal. As a result, the amount of absorption can be significantly affected.

Research in the field of atmospheric infrasound has been highly motivated over the last two decades by the development of the International Monitoring System for the enforcement of the Comprehensive Nuclear-Test-Ban Treaty, which bans all kind of nuclear explosions (Christie & Campus 2010; Brachet *et al.* 2010). In this context, evaluating the importance of absorption and non-linear effects on the signals measured at ground level is crucial to allow a quantitative characterization of the source. Current methods of estimating the size of a source from infrasound data are based on empirical formulae (Mutschlecner & Whitaker 2010), and only a few theoretical investigations have been made on the influence of atmospheric absorption and non-linearity on the amplitude of arrivals. de Groot-Hedlin (2008) simulated the upward propagation of an acoustic signal with and without attenuation. The approach was however based on a linear equation. Rogers & Gardner (1980) performed a theoretical analysis of the interaction between classical absorption and non-linear distortion, and a numerical illustration has been provided by the more recent work of Lonza *et al.* (2015). Nonetheless, both studies neglect the effects of relaxation phenomena.

The direct numerical simulation of the fluid dynamic equations for the study of long-range infrasound propagation in realistic atmospheres is now possible (de Groot-Hedlin *et al.* 2011; Marsden *et al.* 2014; Sabatini *et al.* 2015; de Groot-Hedlin 2016; Sabatini *et al.* 2016), and investigations based on this approach are expected to lead to a better understanding of the inherent physics. The conventional formalism of the Navier–Stokes equations includes viscous, thermal and rotational terms, but does not account for vibrational losses. A complete model incorporating non-equilibrium phenomena was developed by Pierce (1978) and preliminary numerical results on atmospheric acoustic propagation have been shown in the more recent works of Wochner *et al.* (2005) and de Groot-Hedlin (2012), however neither of them focuses on long-range high-altitude infrasound propagation. Including vibrational relaxation not only results in a higher number of equations (Pierce 1978) but may also lead to a severe limitation of the integration time step, which is dependent on the smallest relaxation time of the atmospheric molecules (Hanique-Cockenpot *et al.* 2010).

The goal of this work is the assessment of attenuation and non-linearity on long-range propagation of explosion waves. The objective is twofold. On the one hand, it is necessary to improve our understanding of atmospheric absorption and, in particular, its interaction with non-linear effects, in order to develop better methods of estimating the source strength from infrasound recordings. On the other hand, it appears of primary importance to ascertain whether vibrational relaxation can be reasonably neglected in direct solvers, in order to avoid an excessively large computational cost. For these purposes, the acoustic propagation in a realistic atmosphere of explosion-like waves of frequency in the infrasound range is investigated on stratospheric and thermospheric arrivals for different source amplitudes and frequencies. Non-linear ray theory is employed. In this method, acoustic signals are supposed to propagate along particular paths, known as acoustic rays, which are computed by solving the equations of geometrical acoustics (Candel 1977), whereas the evolution of the amplitude along the rays is modelled by a 1-D transport equation. The augmented Burgers' equation proposed by Cleveland *et al.* (1996) is used here. This methodology appears well suited for the present investigations, as it allows to account for vibrational relaxation, classical absorption and non-linear terms in a straightforward way and with a reduced computational cost, given the uni-dimensional nature of the governing equation. Similar approaches for long-range infrasound propagation can be found in Gainville *et al.* (2006, 2010) and Lonzaga *et al.* (2015). Sonic boom propagation has also been extensively studied using non-linear ray theory (Rogers & Gardner 1980; Cleveland 1995; Rallabhandi 2011; Yamamoto *et al.* 2015).

For the purposes of this study, an infrasonic wave is assumed to be emitted by a fixed point source located at ground level. The initial signature is supposed known at a certain distance from the source location and modelled using the waveform proposed by Reed (1977) for explosions. The mean atmospheric variables are defined from the specification of the vertical profile of speed of sound, which is taken from studies previously performed by the authors (Sabatini *et al.* 2016). The model proposed by Sutherland & Bass (2004) is employed for evaluating the coefficients of the absorption terms. The propagation is analysed on stratospheric and thermospheric rays up to a range of 325 km.

The augmented Burgers' equation is solved numerically via a high-order finite-difference time-domain method (Bogey & Bailly 2004; Berland *et al.* 2006). Acoustic shocks are handled using a shock-capturing procedure based on low-order filtering (Bogey *et al.* 2009), with a new specific shock detector (Sabatini *et al.* 2016). Vi-

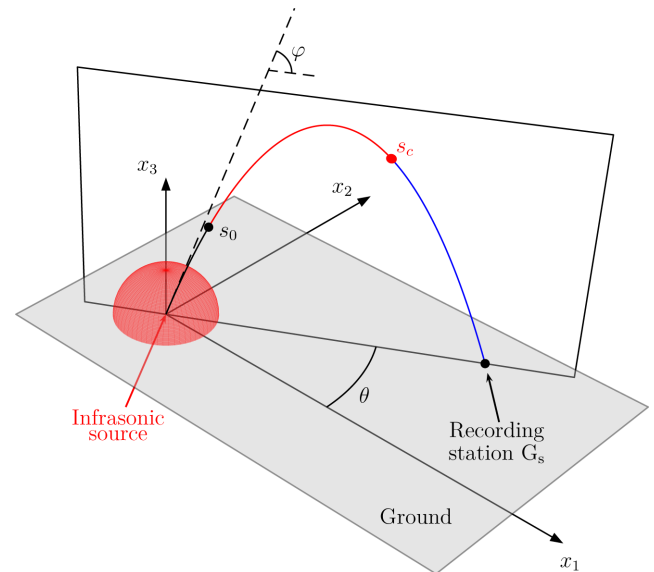


**Figure 1.** Sketch of the physical framework. A point source is placed at the origin of the Cartesian coordinates.

brational relaxation is finally taken into account using the analytical technique recently proposed by Yamamoto *et al.* (2015).

The paper is organized as follows. The acoustic propagation model is presented in Section 2, along with a brief theoretical analysis of the main terms of the augmented Burgers' equation. Numerical issues are discussed in Section 3. Simulation parameters and results are described in Section 4 and concluding remarks are finally drawn in Section 5.

## 2 ACOUSTIC PROPAGATION MODEL

In the geometrical acoustics approximation and in the absence of wind, an acoustic ray  $\mathbf{x}(t)$  is defined by the first-order differential system (Candel 1977)

$$\begin{cases} \frac{d\mathbf{x}}{dt} = \bar{c}\mathbf{n} \\ \frac{d\mathbf{n}}{dt} = (\mathbf{n} \cdot \nabla \bar{c})\mathbf{n} - \nabla \bar{c} \end{cases} \quad (1)$$

where  $\bar{c}$  is the equilibrium speed of sound and  $\mathbf{n}$  is the unit normal to the wavefront. System (1) is to be integrated from an initial surface. For a fixed point source, this surface is a sphere which can be parametrized by the longitude  $\theta$  and the latitude  $\varphi$ , as illustrated in Fig. 1, and a given couple  $(\theta, \varphi)$  corresponds to a unique ray. When no wind is considered, the wavefront remains invariant with respect to any rotation around the vertical axis  $x_3$  and the ray corresponding to the angles  $(\theta, \varphi)$  always lies on the same plane. Thus, it is sufficient to investigate rays emitted with a longitude  $\theta = 0^\circ$ . In this case, the initial conditions needed to solve system (1) are

$$\begin{cases} \mathbf{x}(t=0) = \mathbf{0} \\ \mathbf{n}(t=0) = \cos(\varphi)\mathbf{e}_1 + \sin(\varphi)\mathbf{e}_3. \end{cases} \quad (2)$$

The point source is located at the origin of the frame and  $\mathbf{e}_i$ ,  $i = 1, 2, 3$ , are the unit vectors of the Cartesian coordinate system.

In the weakly non-linear regime, the evolution of a signal  $p(s, t_r)$  along an acoustic ray  $\mathbf{x}(t)$  can be modelled by the

augmented Burgers' equation (Cleveland *et al.* 1996)

$$\begin{aligned} \frac{\partial p'}{\partial s} - \frac{\beta}{2\bar{\rho}\bar{c}^3} \frac{\partial p'^2}{\partial t_r} + \frac{p'}{2A} \frac{\partial A}{\partial s} - \frac{p'}{2\bar{\rho}\bar{c}} \frac{\partial(\bar{\rho}\bar{c})}{\partial s} \\ = \frac{\bar{\mu}_{cl}}{2\bar{\rho}\bar{c}^3} \frac{\partial^2 p'}{\partial t_r^2} + \sum_m \frac{\Delta c_m}{\bar{c}^2} \int_{-\infty}^{t_r} e^{-(t_r-\tau)/\tau_m} \frac{\partial^2 p'}{\partial \tau^2} d\tau \end{aligned} \quad (3)$$

where

$$s \equiv \int_0^{t_r} \left[ \left( \frac{dx_1}{d\tau} \right)^2 + \left( \frac{dx_2}{d\tau} \right)^2 + \left( \frac{dx_3}{d\tau} \right)^2 \right]^{1/2} d\tau \quad (4)$$

is the curvilinear abscissa and  $t_r$  the retarded time

$$t_r = t - \int_{s_0}^s \frac{1}{\bar{c}(\xi)} d\xi \quad (5)$$

with  $s_0$  a reference point on the ray, at which the initial condition  $p'(s = s_0, t_r = t) = q_0(t)$  is specified. In eq. (3),  $\bar{\rho}$  is the mean density and  $\beta = (\gamma + 1)/2$  is the coefficient of non-linearity, where  $\gamma$  represents the ratio of specific heats. When considering only the two first terms, eq. (3) reduces to the well-known lossless 1-D Burgers' equation. The geometrical spreading along the ray is taken into account by the third term. The function  $A(s)$  is related to the elemental ray tube area  $d\Sigma(s) \equiv A(s)d\theta d\varphi$  spanned by the four rays emitted with initial angles  $(\theta, \varphi)$ ,  $(\theta + d\theta, \varphi)$ ,  $(\theta, \varphi + d\varphi)$ ,  $(\theta + d\theta, \varphi + d\varphi)$ , and is defined as

$$A(s) \equiv \|\mathbf{r}_\theta(s) \times \mathbf{r}_\varphi(s)\| \quad (6)$$

where the vectors  $\mathbf{r}_p = \partial \mathbf{x} / \partial p$ , with  $p = \theta$  or  $p = \varphi$ , are the so-called geodesic elements. The fourth term is associated with the inhomogeneities of the medium. Finally, losses are described by the right-hand side of eq. (3). The first term is here referred to as classical diffusion and includes the viscous, thermal and rotational relaxation contributions, respectively, proportional to the dynamic viscosity of the medium  $\bar{\mu}$ , the conductivity  $\bar{\kappa}$  through the Prandtl number  $Pr$  and the bulk viscosity  $\bar{\mu}_b$ . The parameter  $\bar{\mu}_{cl}$  is given by

$$\bar{\mu}_{cl} = \frac{4}{3}\bar{\mu} + \frac{\gamma - 1}{Pr}\bar{\mu} + \bar{\mu}_b. \quad (7)$$

The second term of the right-hand side of eq. (3) represents vibrational relaxation processes. In the integral expression,  $\tau_m$  is the relaxation time relative to the molecule  $m$  and  $\Delta c_m$  a coefficient associated with the increase in the phase speed induced by the relaxation process  $m$ .

The pressure perturbation  $p'$  is generally normalized according to the expression

$$q = \left( \frac{\bar{\rho}_0 \bar{c}_0 A}{\bar{\rho} \bar{c} A_0} \right)^{1/2} p' \quad (8)$$

which compensates for amplitude variations due to geometrical spreading and inhomogeneities of the medium. In eq. (8), the subscript 0 indicates that the corresponding variable is evaluated at the initial abscissa  $s_0$ . Eq. (3) is finally recast as

$$\frac{\partial q}{\partial s} = S_{nl} + S_{cl} + S_{vb} \quad (9)$$

where  $S_{nl}$ ,  $S_{cl}$  and  $S_{vb}$  represent the non-linear, classical dissipation and vibrational relaxation effects,

$$S_{nl} = \frac{\beta_e}{2\bar{\rho}_0\bar{c}_0^3} \frac{\partial q^2}{\partial t_r}, \quad \beta_e = \beta \left( \frac{\bar{\rho}_0 \bar{c}_0^5 A_0}{\bar{\rho} \bar{c}^5 A} \right)^{1/2} \quad (10)$$

$$S_{cl} = \frac{\bar{\mu}_{cl}}{2\bar{\rho}\bar{c}^3} \frac{\partial^2 q}{\partial t_r^2} \quad (11)$$

$$S_{vb} = \sum_m \frac{\Delta c_m}{\bar{c}^2} \int_{-\infty}^{t_r} e^{-(t_r-\tau)/\tau_m} \frac{\partial^2 q}{\partial \tau^2} d\tau \quad (12)$$

and  $\beta_e$  is the so-called coefficient of effective non-linearity.

## 2.1 Analysis of non-linear and absorption terms

When the right-hand side of eq. (9) can be neglected, that is in the case of linear propagation with no absorption mechanism,  $q$  remains constant with  $s$  and the acoustic energy flow rate, which is proportional to  $q^2$ , is conserved along the acoustic ray. Accordingly, the pressure perturbation  $p'$  evolves as  $(\bar{\rho}\bar{c}/A)^{1/2}$ .

More generally, the right-hand side of eq. (9) cannot be neglected. An exact solution of eq. (9) including only the source term  $S_{nl}$  can still be obtained by introducing the variable (Cleveland 1995)

$$\tilde{x}(s) = \int_{s_0}^s \frac{\beta_e(\xi)}{\beta} d\xi \quad (13)$$

eq. (9) can thus be recast as

$$\frac{\partial q}{\partial \tilde{x}} = \frac{\beta}{2\bar{\rho}_0\bar{c}_0^3} \frac{\partial q^2}{\partial t_r} \quad (14)$$

so that, with  $q(\tilde{x} = 0, t_r = t) = q_0(t)$  the initial condition, the exact implicit solution is given by

$$q(\tilde{x}, t_r) = q_0 \left( t_r + \frac{\beta \tilde{x} q(\tilde{x}, t_r)}{\bar{\rho}_0 \bar{c}_0^3} \right). \quad (15)$$

The second term in the argument of  $q_0$  in eq. (15) tends to modify the shape of the wave, and the amount of distortion is linearly dependent on  $\tilde{x}$ . For this reason, the variable  $\tilde{x}$  is often referred to as distortion distance (Cleveland 1995). Furthermore, multivalued solutions can be generated. A single-valued signature is then obtained by introducing shock waves (Hamilton & Blackstock 2008).

In order to get more insight into the analysis of non-linear, classical dissipation and vibrational relaxation effects, it is useful to investigate the evolution along the acoustic ray of the energy  $E(s)$  of the signal  $q$ , which is defined as

$$E(s) \equiv \int_{-\infty}^{+\infty} q^2(s, t_r) dt_r \quad (16)$$

or, equivalently, as

$$E(s) = \int_0^{+\infty} \mathcal{E}_q(s, f) df \quad (17)$$

where  $\mathcal{E}_q(s, f) = 2|\hat{q}(s, f)|^2$  is the one-sided spectrum associated with the Fourier component  $\hat{q}(s, f)$  of frequency  $f$

$$\hat{q}(s, f) = \int_{-\infty}^{+\infty} q(s, t_r) e^{-i2\pi f t_r} dt_r. \quad (18)$$

Hereafter,  $q$  is considered a continuous function of both space and time. With some manipulations of eq. (9) (see Appendix A for further details), it can be shown that the energy spectral density  $\mathcal{E}_q$  is governed by the Lin's equation (Bailly & Comte-Bellot 2015)

$$\frac{\partial \mathcal{E}_q(s, f)}{\partial s} = \frac{\beta_e(s)}{\bar{\rho}_0 \bar{c}_0^3} \mathcal{T}(s, f) + \mathcal{D}(s, f) \quad (19)$$

where  $\mathcal{T}$  and  $\mathcal{D}$  are the so-called non-linear transfer and dissipation terms, respectively. The former takes into account the interaction

among harmonics, which is associated with the waveform distortion during propagation. The latter represents the rate of decay of the spectral component  $\hat{q}(s, f)$  due to the dissipative mechanisms. Integrating eq. (19) over all frequencies provides

$$\frac{dE(s)}{ds} = \frac{\beta_e(s)}{\bar{\rho}_0 \bar{c}_0^3} \int_0^{+\infty} \mathcal{T}(s, f) df + \int_0^{+\infty} \mathcal{D}(s, f) df. \quad (20)$$

As demonstrated in Appendix A, the first term at the right-hand side of eq. (20) is identically zero. Consequently, the non-linear transfer function  $\mathcal{T}$  is only responsible for a redistribution of energy among spectral components, but does not affect the total energy  $E$ . The dissipation function  $\mathcal{D}$  can be written as

$$\mathcal{D}(s, f) = -2\alpha(s, f)\mathcal{E}_q(s, f). \quad (21)$$

The coefficient  $\alpha = \alpha_{cl} + \alpha_{vb}$  contains both the classical and vibrational relaxation contributions

$$\alpha_{cl}(s, f) = \frac{\bar{\mu}_{cl}(s)(2\pi f)^2}{2\bar{\rho}(s)\bar{c}(s)^3} \quad (22)$$

$$\alpha_{vb}(s, f) = \sum_m \frac{2\pi f_m(s)\Delta c_m(s)}{\bar{c}^2(s)} \frac{(f/f_m(s))^2}{1 + (f/f_m(s))^2} \quad (23)$$

where  $f_m = 1/(2\pi\tau_m)$  is the relaxation frequency of the molecule  $m$ . For a given point  $s$  on the acoustic ray, the term  $\alpha_{cl}$  is proportional to  $f^2$ , indicating a quadratic increase of classical absorption with frequency. On the other hand, the coefficient  $\alpha_{vb}$  reaches significant values only for Fourier components of frequency around  $f_m$ , whereas it is practically negligible for  $f > 10^2 f_m$  or  $f < 10^{-2} f_m$ .

The vibrational source term  $S_{vb}$  also induces dispersion (Hamilton & Blackstock 2008). More specifically, the phase speed  $c_\varphi$  can be computed from its Taylor series

$$c_\varphi = \bar{c} + \sum_m \left[ \frac{(f/f_m)^2}{1 + (f/f_m)^2} \Delta c_m + \mathcal{O}(\Delta c_m^2) \right]. \quad (24)$$

This velocity increases monotonically from its equilibrium value  $\bar{c}$  to the frozen speed of sound  $\bar{c} + \sum_m \Delta c_m$ . As will be shown in Section 4.2, this effect is very weak in the infrasound frequency range.

The behaviour of the coefficient of absorption  $\alpha$  and the phase speed  $c_\varphi$  in a realistic atmosphere will be discussed in Section 4.

Finally, it is worth noting that, in the present model, ray paths are computed using the equilibrium value  $\bar{c}$  of the speed of sound. Consequently, they depend neither on the amplitude of the wave nor on the frequency. This is in general not true for finite-amplitude signals propagating in a dispersive medium. Nevertheless, in the weakly non-linear regime and for weakly dispersive media, the error induced by this assumption is expected to be small. A more detailed discussion on this topic can be found in Hamilton & Blackstock (2008).

### 3 NUMERICAL INTEGRATION

The numerical algorithm involves two main steps. First, the eigenrays connecting the source with a given receiver are computed, along with the corresponding curvilinear abscissa  $s$  and the spreading term  $A/A_0$ . Second, the augmented Burgers' equation is integrated along each ray. The acoustic pressure at the recording station is then obtained by the sum of each ray contribution. In this section, the numerical procedure employed in each step is briefly described, and the algorithm is then validated with the case of a step shock propagating in a monorelaxing fluid.

#### 3.1 Computation of eigenrays, curvilinear abscissa and spreading term

The computation of the eigenrays connecting the source with a given receiver  $P = G_s$  consists in determining angles  $\varphi$  for which the distance  $d(\varphi) = ||P(\varphi) - G_s||$  becomes nil. In this work, a grid of discrete values  $\varphi_i$  is constructed. For each  $\varphi_i$ , the ray  $\mathbf{x}(t; \varphi_i)$  is calculated by solving systems (1) and (2) using the low-dissipation and low-dispersion fourth-order Runge–Kutta scheme proposed by Berland *et al.* (2006). An approximation of the function  $d(\varphi)$  is thus obtained. The eigenrays are then given by the zeros of  $d(\varphi)$ . For each of them, the curvilinear abscissa  $s$  is computed by eq. (4). Concerning the spreading term  $A/A_0$ , it is straightforward to show that, for  $\theta = 0^\circ$  and under the hypothesis of rotational symmetry around the vertical axis  $x_3$ , the vector  $\mathbf{r}_\theta$  is perpendicular to the  $x_1x_3$ -plane and equal to  $\mathbf{r}_\theta = x_1\mathbf{e}_2$ . Following Candell (1977), the geodesic element  $\mathbf{r}_\varphi$  can be obtained by integrating the differential system

$$\begin{cases} \frac{d\mathbf{r}_\varphi}{dt} = (\mathbf{r}_\varphi \cdot \nabla \bar{c}) \mathbf{n} + \bar{c} \mathbf{n}_\varphi \\ \frac{d\mathbf{n}_\varphi}{dt} = (\mathbf{n} \cdot \nabla \bar{c}) \mathbf{n}_\varphi + (\mathbf{n}_\varphi \cdot \nabla \bar{c}) \mathbf{n} - [\mathbf{v}_\varphi - (\mathbf{n} \cdot \mathbf{v}_\varphi) \mathbf{n}] \end{cases} \quad (25)$$

where  $\mathbf{v}_\varphi = (\mathbf{r}_\varphi \cdot \nabla) \nabla \bar{c}$ , with the initial conditions  $\mathbf{r}_\varphi(0) = \mathbf{0}$  and  $\mathbf{n}_\varphi(0) = -\sin(\varphi)\mathbf{e}_1 + \cos(\varphi)\mathbf{e}_3$ . The ray tube area  $A$  is finally given by eq. (6). As an illustration, when  $\bar{c}$  is constant throughout the medium, rays are straight lines, the derivative of the unit vector  $\mathbf{n}_\varphi$  remains constant and  $\mathbf{r}_\varphi = \bar{c}t\mathbf{n}_\varphi$ , so that  $A(s) = \bar{c}t x_1 = (\bar{c}t)^2 \cos(\varphi)$ , as expected for a configuration with spherical symmetry.

#### 3.2 Integration of the generalized Burgers' equation

The ray tube area  $A$  may vanish along the acoustic rays for an inhomogeneous medium. The locus of points  $s_c$  where  $A$  becomes nil is called caustic (Kravtsov & Orlov 1993). In the atmospheric propagation field, fold and cusp caustics are commonly encountered. The effect of such singularities on the waveform is not directly taken into account by the augmented Burgers' equation and an *ad-hoc* treatment is required. For the purpose of this study, as suggested by Rogers & Gardner (1980), a phase shift is applied to the acoustic signal every time a caustic is crossed. If  $q_{in}(t_r) = q(s_c, t_r)$  is the incoming waveform, the outgoing signal  $q_{out}(t_r)$  is computed as the Hilbert transform of  $q_{in}(t_r)$

$$q_{out}(t_r) = -\frac{1}{\pi} \int_{-\infty}^{+\infty} \frac{q_{in}(\tau)}{\tau - t_r} d\tau. \quad (26)$$

Moreover, at the caustic point  $s_c$ , the generalized Burgers equation cannot be directly integrated in the form (9) as the coefficient  $\beta_e$  becomes infinite. For this reason, Gainville (2008) proposed to define the following new variable  $\eta = |s - s_c|^{1/2}$ . Hence, eq. (9) is recast as

$$\frac{\partial q}{\partial \eta} = \text{sgn}(s - s_c) \eta \frac{\beta_e}{\bar{\rho}_0 \bar{c}_0^3} \frac{\partial q^2}{\partial t_r} + 2 \text{sgn}(s - s_c) \eta [S_{cl} + S_{vb}]. \quad (27)$$

In the neighbourhood of the fold or cusp caustics,  $A(s) = A'(s_c)(s - s_c) + \mathcal{O}((s - s_c)^2)$ , so that the coefficient of the non-linear term remains finite at  $s = s_c$ . In practice, the acoustic ray is divided into two segments, to the left and the right of the caustic point, respectively (see Fig. 1). Eq. (27) is integrated on the left-hand side from  $\eta_0 = |s_0 - s_c|^{1/2}$  to  $\eta = 0$ . The Hilbert transform (26) is then

applied to the temporal signal  $q(\eta = 0, t_r)$  obtained at  $s = s_c$  and the result is used as the initial condition for the integration of eq. (27) on the right-hand side from  $\eta = 0$  to the recording station  $G_s$ .

The integration of eq. (27),  $\partial q / \partial \eta = \mathcal{F}(\eta, q)$ , is performed on both segments using the low-dissipation and low-dispersion fourth-order Runge–Kutta scheme developed by Berland *et al.* (2006). At each stage of the Runge–Kutta algorithm, the temporal derivative of the non-linear term is computed on a regular grid with time step  $\Delta t_r$  using an explicit fourth-order 11-point stencil centred scheme optimized to reduce the dispersion error (Bogey & Bailly 2004). The viscous term is computed with a standard second-order centred scheme. Vibrational relaxation effects are calculated using the technique recently proposed by Yamamoto *et al.* (2015). The relaxation term (12) is rewritten in the form (Pierce 1985)

$$S_{vb}(\eta, q) = \sum_m \frac{\Delta c_m}{\bar{c}^2} \frac{\partial q_m}{\partial t_r} \quad (28)$$

where the auxiliary variables  $q_m$  satisfy the expression

$$\left( \frac{1}{\tau_m} + \frac{\partial}{\partial t_r} \right) q_m = \frac{\partial q}{\partial t_r}. \quad (29)$$

Eq. (29) has the following solution

$$q_m(\eta, t_r) = e^{-t_r/\tau_m} q_m(\eta, -\infty) + \int_{-\infty}^{t_r} e^{-(t_r-\tau)/\tau_m} \frac{\partial q}{\partial \tau} d\tau \quad (30)$$

which can be rewritten as

$$q_m(\eta, t_r) = e^{-\Delta t_r/\tau_m} q_m(\eta, t_r - \Delta t_r) + I(\eta, t_r) \quad (31)$$

with

$$I(\eta, t_r) = \int_{t_r - \Delta t_r}^{t_r} e^{-(t_r-\tau)/\tau_m} \frac{\partial q}{\partial \tau} d\tau. \quad (32)$$

Replacing the exponential function in the integral by its mean over the interval  $[t_r - \Delta t_r, t_r]$ , the values of  $q_m$  can be explicitly computed as

$$q_m(\eta, t_r) = e^{-\Delta t_r/\tau_m} q_m(\eta, t_r - \Delta t_r) + I_a(\eta, t_r) \quad (33)$$

where

$$I_a(\eta, t_r) = e^{-\Delta t_r/(2\tau_m)} [q(\eta, t_r) - q(\eta, t_r - \Delta t_r)]. \quad (34)$$

The derivatives  $\partial q_m / \partial t_r$  are then calculated with the same fourth-order scheme used for the non-linear term  $S_{nl}$ . For an harmonic wave of the form  $q = e^{-i\omega t_r}$ , the error  $|I - I_a|$  is given by

$$|I - I_a| = \frac{\omega (1 + 4\omega^2 \tau_m^2)^{1/2}}{24\tau_m^2} \Delta t_r^3 + \mathcal{O}(\Delta t_r^4) \quad (35)$$

which means that the approximation  $I_a$  of the integral  $I$  is formally of third order in  $\Delta t_r$ . Contour lines of the relative error  $\epsilon_I = |I - I_a|/|I|$  are plotted in Fig. 2 as a function of the dimensionless angular frequency  $\omega \Delta t_r$  and the ratio  $\Delta t_r/\tau_m$ . The line  $\omega \Delta t_r = \omega_a \Delta t_r$ , with  $\omega_a \Delta t_r = 2\pi/5$ , corresponding to the accuracy limit of the fourth-order finite-difference scheme used for derivatives with respect to the variable  $t_r$  (Bogey & Bailly 2004), is also reported. As an illustration, for  $\Delta t_r = 0.1 \tau_m$ ,  $\epsilon_I$  is always lower than 1 percent for frequencies smaller than  $\omega_a \Delta t_r$ .

Grid-to-grid oscillations are not resolved by centred finite-difference schemes and can be removed using a low-pass selective filter with cut frequency close to  $(\omega \Delta t_r)_a$  (Bogey & Bailly 2004).

Finally, to handle acoustic shocks, a shock-capturing technique is employed (Bogey *et al.* 2009). The methodology consists in applying artificial dissipation only near shock fronts and involves

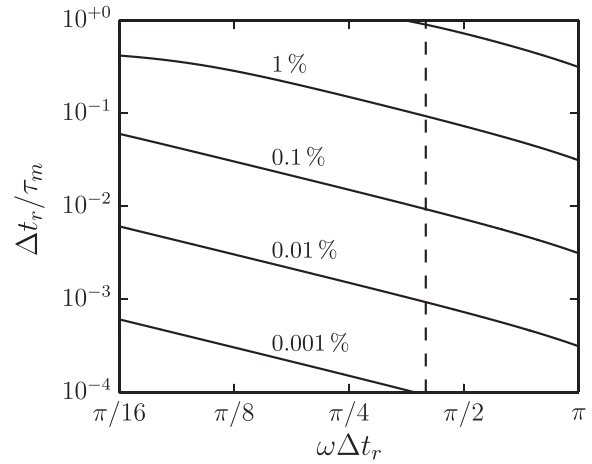


**Figure 2.** Relative error  $\epsilon_I = |I - I_a|/|I|$  as a function of the non-dimensional angular frequency  $\omega \Delta t_r$  and the ratio  $\Delta t_r/\tau_m$ . The dashed vertical line represents a resolution limit of 5 points per period.

two main steps. The locations of the discontinuities are first determined through a shock sensor. To this end, a new detector has been specifically developed for acoustic applications (Sabatini *et al.* 2016). Then, a second-order filter is applied in conservative form with a strength which is significant around the shocks but nil everywhere else. In this way, smooth regions of the solution remain unaffected.

### 3.3 Validation of the numerical procedure

In order to illustrate the capabilities of the present algorithm, the plane wave propagation of a step shock in a mono-relaxing inviscid and homogeneous fluid is investigated. Under these assumptions, eq. (3) reduces to

$$\frac{\partial P}{\partial \zeta} = \frac{1}{2} \frac{\partial P^2}{\partial \theta_r} + \mathcal{R} \int_{-\infty}^{\theta_r} e^{-(\theta_r - \chi)/\Theta_1} \frac{\partial^2 P'}{\partial \chi^2} d\chi \quad (36)$$

with  $P = p'/\bar{p}_0$ ,  $\zeta = s/s_{nl}$ ,  $\theta_r = \omega t_r$ ,  $\Theta_1 = \omega \tau_1$  and  $\mathcal{R} = (\Delta c_1 \bar{\rho}_0 \bar{c}_0)/(\beta \bar{p}_0)$ , where  $\bar{p}_0$  is the ambient pressure,  $s_{nl}$  the so-called shock formation distance and  $1/\omega$  a characteristic timescale. The coefficient  $\mathcal{R}$  represents a measure of the relative importance between relaxation and non-linear effects. The initial signature is a pressure jump of  $2\bar{p}_0$ , from  $-\bar{p}_0$  ahead of the wavefront ( $t_r \in ]-\infty, 0[$ ) to  $+\bar{p}_0$  behind ( $t_r \in ]0, +\infty[$ ). For large propagation distances, eq. (36) has a closed-form stationary wave solution ( $\partial P / \partial \zeta = 0$ ) given by the following implicit expression (Cleveland *et al.* 1996; Hamilton & Blackstock 2008)

$$\theta_r = \Theta_1 \log \left[ \frac{(1 + P)^{\mathcal{R}-1}}{(1 - P)^{\mathcal{R}+1}} \right] + \text{constant}. \quad (37)$$

For  $\mathcal{R} < 1$ , eq. (37) describes a multivalued waveform, which can be corrected using weak-shock theory. The peak shock pressure is  $P_s = (1 - 2\mathcal{R})$ . To validate the numerical procedure, an investigation is performed for  $\mathcal{R} = 0.5$  and  $\Theta_1 = 1/6$ . The computation is carried out on a uniform grid of spacing  $\Delta \theta_r = 5.29 \times 10^{-5}$ . The result obtained at  $\zeta = 5$  is illustrated in Fig. 3(a), along with the analytical multivalued solution. An excellent agreement is found, both for the smooth non-zero part of the wave and the position of the shock.

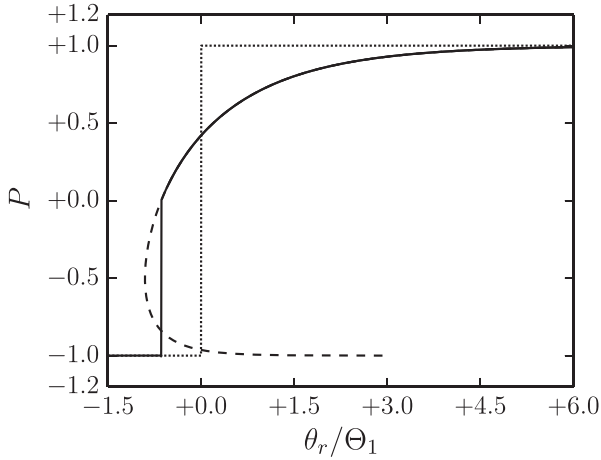


**Figure 3.** Stationary waves in a monorelaxing fluid. Numerical solution for  $\mathcal{R} = 0.5$  and  $\Theta_1 = 1/6$  at  $\xi = 5$  (solid line), initial temporal signature (dotted line) and analytical multivalued solution (dashed line).

#### 4 A NUMERICAL INVESTIGATION OF RELAXATION EFFECTS ON INFRASONIC WAVES

Using the methodology presented in the previous section, an analysis of the long-range atmospheric propagation of explosion-like waves is carried out. In this section, the mean atmospheric state, the source signature and the simulation parameters are first presented. Results are then illustrated and discussed.

##### 4.1 Atmosphere

The mean atmospheric field is a vertically stratified medium. The speed of sound  $\bar{c} = \bar{c}(x_3)$  is here defined as the effective celerity obtained from data observed during the *Misty Picture experiment* in the east–west direction (Gainville *et al.* 2010). The numerical values have been taken from previous investigations performed by the authors (Sabatini *et al.* 2016). This profile, displayed in Fig. 4(a), induces two main waveguides. First, a stratospheric duct, located between the ground and the altitude of the first local maximum of  $\bar{c}$ , around  $x_3 = 53.5$  km. Second, a thermospheric waveguide, between the Earth’s surface and the altitude at which  $\bar{c}$  reaches its ground-level value, that is  $x_3 = 105$  km. The mean temperature  $\bar{T}(x_3)$  is computed from the speed of sound according to  $\bar{T}(x_3) = \bar{c}^2(x_3)/(\gamma r_M)$ , where  $r_M$  is the specific gas constant, whereas the mean pressure  $\bar{p}(x_3)$  is obtained by solving the hydrostatic equilibrium equation

$$\frac{d\bar{p}}{dx_3} = -\bar{\rho}g = -\frac{g}{r_M\bar{T}}\bar{p} \quad (38)$$

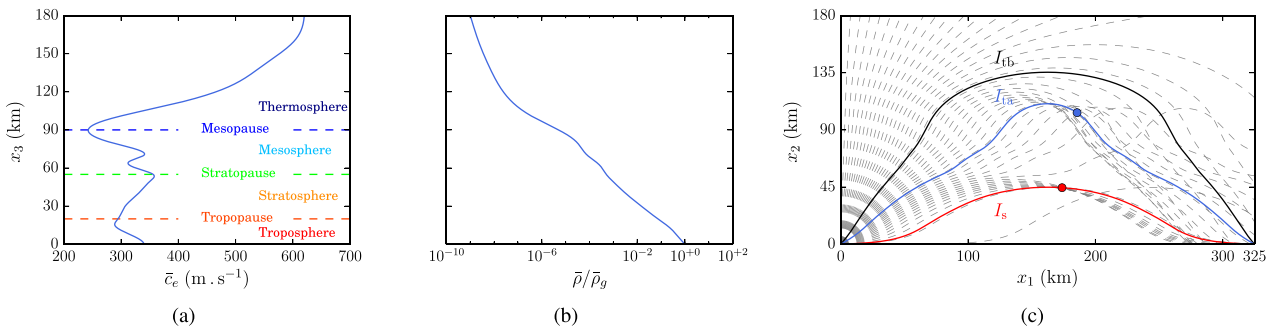


**Figure 4.** (a) Atmospheric speed of sound  $\bar{c}$  as a function of the altitude  $x_3$ . (b) Atmospheric density  $\bar{\rho}$  normalized with respect to its value at ground level  $\bar{\rho}_g$  as a function of the altitude  $x_3$ . (c) Eigenrays connecting the point source with a ground-level barometric station located at  $x_1 = 325$  km.

where  $g = 9.81 \text{ m s}^{-2}$  is the gravitational acceleration. Eq. (38) is integrated numerically from  $x_3 = 0$  km with the ground-level pressure fixed to  $\bar{p}_g = 101325$  Pa. Finally, the density profile  $\bar{\rho}$  is obtained from the equation of state  $\bar{\rho} = \bar{p}/(r_M\bar{T})$  and is plotted in Fig. 4(b). It is worth emphasizing the severe reduction with height of the mean density: at the limit of the thermospheric waveguide,  $\bar{\rho}$  is about 8 orders of magnitude smaller than its value at the Earth’s surface.

##### 4.2 Absorption and dispersion terms

The mean dynamic viscosity  $\bar{\mu}$  is provided by the Sutherland’s law

$$\bar{\mu}(x_3) = \bar{\mu}_{\text{ref}} \left( \frac{\bar{T}(x_3)}{\bar{T}_{\text{ref}}} \right)^{3/2} \frac{\bar{T}_{\text{ref}} + \bar{S}}{\bar{T}(x_3) + \bar{S}} \quad (39)$$

where  $\bar{\mu}_{\text{ref}} = 1.8192 \times 10^{-5} \text{ kg m}^{-1} \text{ s}^{-1}$ ,  $\bar{T}_{\text{ref}} = 293.15 \text{ K}$  and  $\bar{S} = 117 \text{ K}$ . The bulk viscosity  $\bar{\mu}_b$  in eq. (7) is taken as a fraction of the dynamic viscosity  $\bar{\mu}$ , namely  $\bar{\mu}_b(x_3) = 0.6\bar{\mu}(x_3)$  (Pierce 1985). The main contribution to relaxation attenuation is due to the vibration of oxygen  $\text{O}_2$ , nitrogen  $\text{N}_2$ , carbon dioxide  $\text{CO}_2$  and ozone  $\text{O}_3$ . The values of the relaxation times  $\tau_m(x_3)$  and speed of sound increments  $\Delta\bar{c}_m(x_3)$  for these molecules are computed using the expressions provided in Sutherland & Bass (2004). The attenuation coefficient  $\alpha$  obtained with the present modelling is plotted in Fig. 5(a) as a function of the frequency  $f$  and the altitude  $x_3$ . Some contour lines of the ratio  $\alpha_{\text{cl}}/\alpha_{\text{vb}}$  are also reported to highlight the regions of relative importance of classical and vibrational relaxation mechanisms. For infrasound frequencies up to about 10 Hz, classical losses are found to be dominant in the upper atmosphere, above approximately 60 km altitude, mainly as a result of the exponential-like decrease of the atmospheric density. As an example, for  $f = 0.1$  Hz, the coefficient  $\alpha_{\text{cl}}$  is about  $0.45 \text{ dB km}^{-1}$  at  $x_3 = 140$  km, which implies an amplitude diminution of 1 per cent over a range of only 0.2 km. On the other hand, in the troposphere and stratosphere, attenuation is mostly due to the vibrational relaxation of the gas molecules, but the coefficient  $\alpha_{\text{vb}}$  is quite small for frequencies below approximately 1 Hz. These trends can be also observed in Fig. 5(b), where the contributions of  $\alpha_{\text{cl}}$  and  $\alpha_{\text{vb}}$  are shown for three different frequencies,  $f = 0.1, 1, 10$  Hz. For the lowest frequency,  $f = 0.1$  Hz, the vibrational attenuation is of the order  $10^{-4} \text{ dB km}^{-1}$  on average between the ground and 60 km altitude. Consequently, a propagation distance of about  $10^3$  km would be necessary for an amplitude reduction of 1 per cent. The vibrational relaxation attenuation globally increases with frequency in the stratosphere and troposphere. As an illustration, for  $f = 10$  Hz,  $\alpha_{\text{vb}}$  is approximately  $10^{-2} \text{ dB km}^{-1}$  on average below the mesosphere, with a peak of  $10^{-1} \text{ dB km}^{-1}$  at about 10 km altitude.

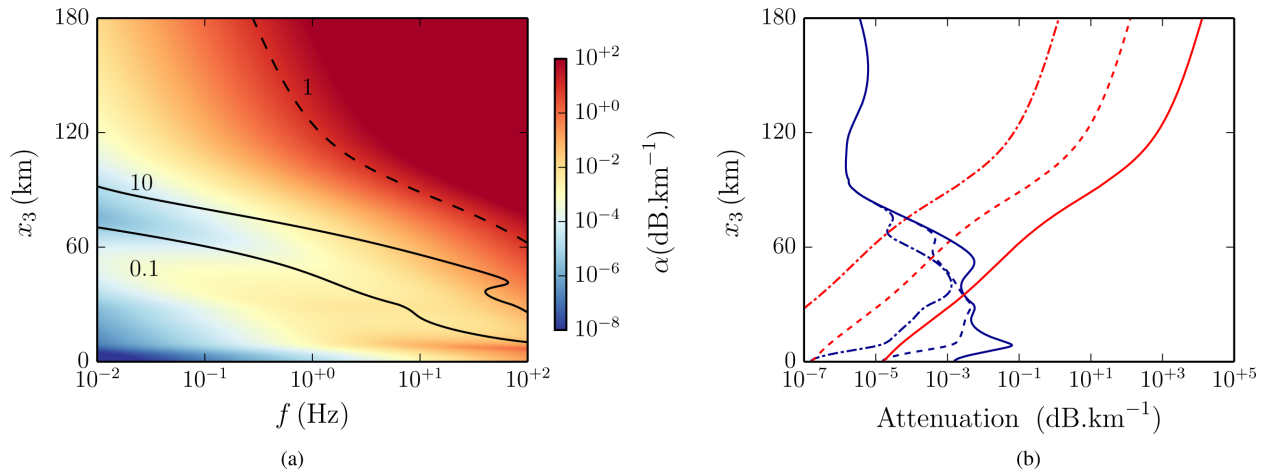


**Figure 5.** (a) Attenuation coefficient  $\alpha$  in  $\text{dB km}^{-1}$  as a function of the frequency  $f$  and the altitude  $x_3$ . --- Contour line  $\alpha = 1 \text{ dB km}^{-1}$ . — Contour lines of  $\alpha_{cl}/\alpha_{vb}$ . (b) Attenuation coefficients  $\alpha_{vb}$  (blue lines) and  $\alpha_{cl}$  (red lines) as functions of the altitude  $x_3$  for  $f = 0.1 \text{ Hz}$  (dash-dotted lines),  $f = 1 \text{ Hz}$  (dashed lines) and  $f = 10 \text{ Hz}$  (solid lines).

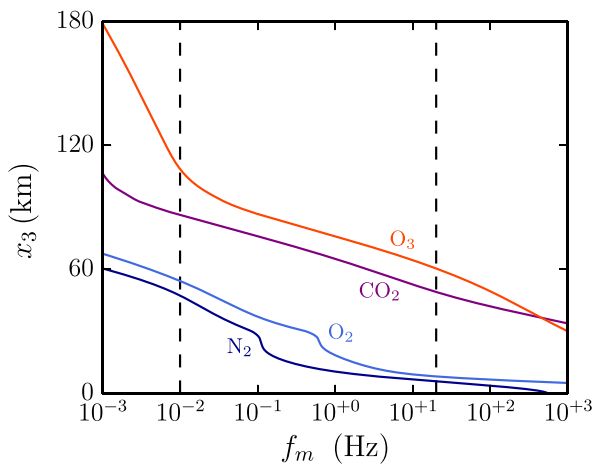


**Figure 6.** Vibrational relaxation frequencies  $f_m$  of oxygen  $\text{O}_2$ , nitrogen  $\text{N}_2$ , carbon dioxide  $\text{CO}_2$  and ozone  $\text{O}_3$  as functions of altitude  $x_3$ . The dashed lines indicate a reference infrasound range [0.01 Hz, 20 Hz].

The relaxation frequencies  $f_m$  of the four molecules considered here are plotted in Fig. 6 as functions of the altitude  $x_3$ . As the absorption reaches its maximum for frequencies closer to the relaxation frequencies, it is expected that the most important contribution to the attenuation of infrasound below the stratospheric limit is provided by the relaxation processes of nitrogen and oxygen.

The dispersion induced by the vibrational relaxation term is weak. As an example, in the infrasound frequency range, the ratio  $c_\varphi/\bar{c}$  predicted by the model of Sutherland and Bass (Sutherland & Bass 2004) is always smaller than  $7 \times 10^{-3}$  below 140 km altitude.

Vibrational relaxation is the sole mechanism responsible for dispersion in the present model. The term  $S_{cl}$  represents in fact an approximation of the classical mechanisms and does not include dispersive effects (Rayleigh 1878; Pierce 1985). Sutherland & Bass (2004), Bass *et al.* (2007) and de Groot-Hedlin (2008) have however pointed out that rotational relaxation may induce an augmentation of the propagation velocity, which is expected to be significant above 100 km altitude and increasingly important with frequency. Using a linear propagation model, Bass *et al.* (2007) have also emphasized that the spectral components affected by this velocity increment are also the most attenuated by classical absorption.

Consequently, they have concluded that rotational relaxation dispersion should not be observed in practice. Furthermore, for the case of acoustic waves produced by explosions at ground level, it can be argued that this dispersive effect is unlikely also as a result of non-linearities. In fact, as will be shown in Section 4.5, infrasound signals lengthen while propagating from the ground to the thermosphere and their spectrum is shifted towards lower frequencies, which are less affected by dispersion.

### 4.3 Initial signature

In order to integrate the augmented Burgers equation (9), an initial condition  $q_0$  must be specified. For the purposes of this study, the signature  $q_0$  is supposed known at a distance  $r = 4 \text{ km}$  from the source and modelled using the waveform proposed by Reed (1977) for explosions

$$q_0(t) = Q_0 \left(1 - \frac{t}{T_+}\right) \left(1 - \frac{t}{T_0}\right) \left[1 - \left(\frac{t}{T_0}\right)^2\right] \Pi_{[0, T_0]}(t) \quad (40)$$

where  $Q_0$  is the initial amplitude,  $T_0$  the total duration of the pulse,  $T_+$  the positive phase duration and  $\Pi_{[0, T_0]}$  the boxcar function. The coefficient  $T_+$  is set to  $7T_0/25$  in order for the integral of  $g$  over time to be nil. The parameters  $Q_0$  and  $T_+$  primarily depend on the so-called source yield  $W$ , which represents the ratio between the energy of the actual explosion and the energy of a reference explosion of 1 kg of trinitrotoluene. As suggested by Gainville *et al.* (2010), the following expressions for  $Q_0$  and  $T_+$ , derived by fitting the tabulated data given by Kinney & Graham (1985), are employed:  $Q_0 = 0.82 \text{ m} \times \bar{p}_g z^{-1}$  and  $T_+ = 0.0041 \text{ s} \times (2W)^{1/3}$  with  $z = r/(2W)^{1/3}$  a scaled distance and  $\bar{p}_g = 101325 \text{ Pa}$  the atmospheric pressure at ground level. A factor 2 for the source yield  $W$  is introduced for explosions located at ground level. The initial signature  $q_0$  normalized with respect to its amplitude  $Q_0$  is plotted in Fig. 7(a) as a function of the non-dimensional time  $t/T_0$ . The pressure disturbance exhibits a shock at  $t/T_0 = 0$  followed by a smooth negative phase before reaching its equilibrium value at  $t/T_0 = 1$ . The corresponding one-sided energy spectral density  $\mathcal{E}_q$  is shown in Fig. 7(b) as a function of the non-dimensional frequency  $fT_0$ . The frequency  $f_p$  of the maximum  $\mathcal{E}_q$  is around  $f_p T_0 \simeq 0.85$  and about 91 per cent of the total energy of the signal is contained in the frequency range  $[0, 6f_p]$ .

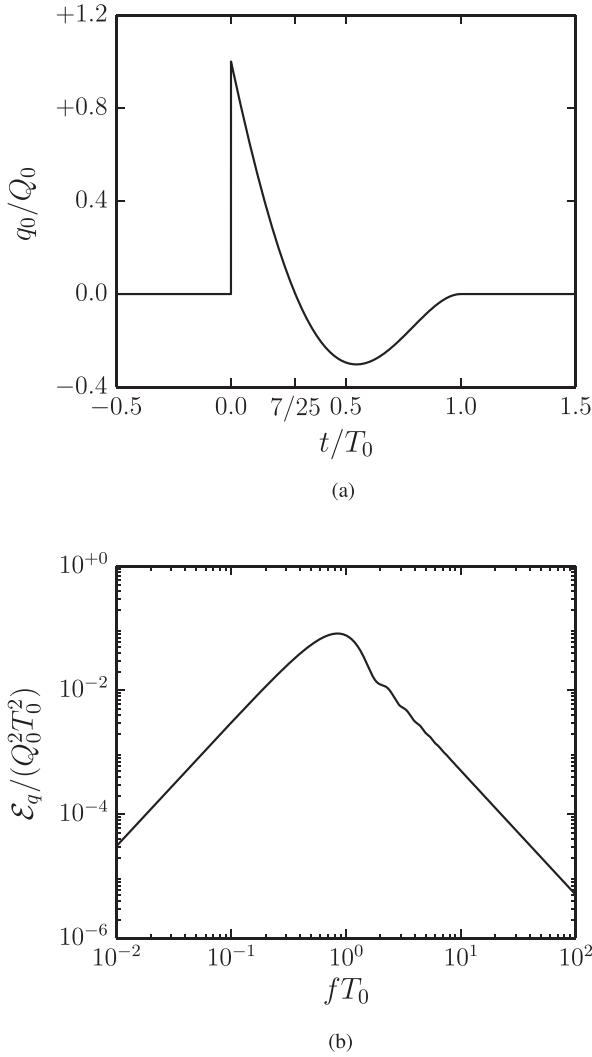


**Figure 7.** (a) Initial signature  $q_0$  normalized with respect to its amplitude  $Q_0$ , see eq. (40). (b) One-sided energy spectral density  $\mathcal{E}_q$  of the initial waveform  $q_0$ .

**Table 1.** Amplitude  $Q_0$ , total duration  $T_0$ , positive phase duration  $T_+$  and central frequency  $f_p$  for three different source yields  $W$ .

Case	$W$	$Q_0$ (Pa)	$T_0$ (s)	$T_+$ (s)	$f_p$ (Hz)
A	$4 \times 10^6$	$4.154 \times 10^3$	2.930	0.8204	0.29
B	$4 \times 10^3$	$4.154 \times 10^2$	0.293	0.0820	2.90
C	$4 \times 10^1$	$8.950 \times 10^1$	0.063	0.0176	13.5

#### 4.4 Simulation parameters

The signal recorded at  $G_s = (325, \text{km}, 0 \text{ km}, 0 \text{ km})$  is investigated for three different values of  $W$ , see Table 1. The three cases will be referred to as *A*, *B* and *C*, respectively. The corresponding amplitudes and central frequencies are representative of a wide range of impulsive sources, from volcanic eruptions (Ripepe & Marchetti 2002) to large explosions (Gainville *et al.* 2010).

The speed of sound profile  $\bar{c}$  chosen for this study induces two caustics, respectively, located in the stratosphere and lower thermosphere. Three rays are found to connect the source with the barometric station  $G_s$ . The lower, emitted with a latitude angle of  $\varphi \simeq 2.496^\circ$ , reaches heights of about 45 km and crosses the stratospheric caustic. Two upper rays climb up to altitudes of 110.6 and

135.4 km before turning back toward the Earth's surface. They are emitted with latitude angles of  $\varphi \simeq 30.23^\circ$  and  $\varphi \simeq 50.23^\circ$ , respectively (Fig. 4). Finally, only the lower thermospheric ray crosses the thermospheric caustic, whereas the ray tube area does not vanish on the highest eigenray.

The present simulations are performed with a constant time step  $\Delta t_r$ , which depends on the highest frequency  $\omega_a \Delta t_r$  to accurately resolve. As an illustration, following the considerations drawn in the previous paragraph,  $f_a = \omega_a / (2\pi)$  could be taken equal to  $f_a = 20f_p$  and would be about 270 Hz for case *C*. By considering a resolution limit of 5 points per period for the finite-difference scheme employed here, the maximum value of  $\Delta t_r$  would be around  $7.4 \times 10^{-4}$  s. For case *C*,  $\Delta t_r$  is set to  $10^{-4}$  s, so that  $f_a = 2$  kHz. As discussed in Section 3, the source term  $S_{vb}$  may not be properly computed in regions of the acoustic ray where  $\tau_m(s) < \Delta t_r$ . In these zones, the spectral components of the signal which are affected by vibrational relaxation have however negligible energy and are removed by the selective filtering procedure.

For the present computations, the spacing  $\Delta \eta$  is constrained for stability reasons by the maximum value of the total kinematic viscosity  $\bar{\nu}_{cl} = \bar{\mu}_{cl} / \bar{\rho}$ , which reaches very high values on the thermospheric rays. In order to avoid an excessive computational cost, the spatial step  $\Delta \eta$  is progressively reduced along these rays in order to meet the stability requirements. As an illustration, for case *B*,  $\Delta \eta$  varies between  $3 \times 10^{-3}$  and  $3 \times 10^{-4}$  m<sup>1/2</sup> on the segment before the caustic point of the lower thermospheric ray.

A final remark concerns the boundary conditions. Before the caustic point, the signal  $q(\eta, t_r)$  has a compact support, so that it is sufficient to consider a domain  $[\min t_r, \max t_r]$  which includes the pulse and impose  $q = 0$  at the boundaries. After performing the Hilbert transformation at the caustic point, the function  $q_{out}(\eta_c, t_r)$  has an asymptotic behaviour of the form

$$q_{out}(\eta_c, t_r) \sim \frac{\chi_0}{t_r} + \frac{\chi_1}{t_r^2} + \dots \quad |t_r| \rightarrow \infty \quad (41)$$

where  $\chi_i$ ,  $i = 0, 1, \dots$ , indicate the moments of  $q_{out}(\eta_c, t_r)$ . Thus, for  $s > s_c$ , function  $q$  slowly goes to zero for  $|t_r| \rightarrow \infty$  and problems can arise when truncating the computational domain. No exact conditions are known, at least to the best of our knowledge. In this work, the following strategy is adopted. Assuming that the mean of the signal remains zero up to  $\eta_c$ ,  $\chi_0 = 0$  and  $q_{out}(\eta_c, t_r) \sim 1/t_r^2$ . For this reason, beyond the caustic point, it is imposed that  $\partial q / \partial t_r + 2q/t_r = 0$  at the boundaries. These conditions are however applied sufficiently far in order for the central part of the signal to be unaffected by possible errors near the boundaries.

## 4.5 Results

### 4.5.1 Case A

The pressure signal computed at the recording station  $G_s$  is plotted in Fig. 8. Results obtained with source terms  $S_{nl}$  and  $(S_{nl} + S_{cl})$  are also shown for comparison. The three curves are nearly superimposed, which means that the evolution of the waveform is essentially driven by non-linear effects. The dissipation term is responsible for the absorption of high frequencies, which are concentrated around the shock regions.

Two different arrivals are clearly visible. The stratospheric phase, referred to as  $I_s$ , is observed between about  $t = 1040$  and  $1060$  s and exhibits a U-shaped waveform, as expected for an N wave crossing a caustic. The corresponding maximum overpressure is around 28 Pa. The second arrival is recorded between about  $t = 1160$  and  $1300$  s

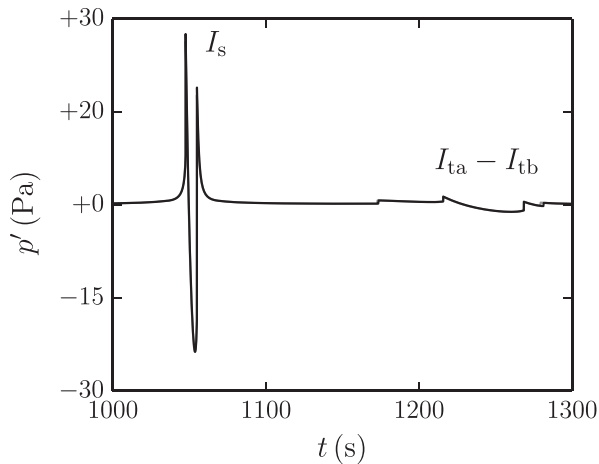


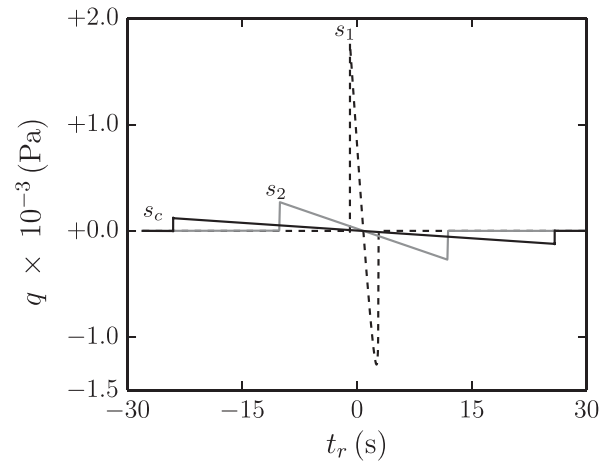
**Figure 8.** Signals  $p'$  recorded at  $G_s$  in case  $A$  with  $(S_{nl})$  (black dashed line),  $(S_{nl} + S_{cl})$  (grey line) and  $(S_{nl} + S_{cl} + S_{vb})$  (black line). The three curves are nearly superimposed.

and is a combination of the lower and upper thermospheric phases, respectively, labelled  $I_{ta}$  and  $I_{tb}$ . The former has a U-shaped waveform, whereas the latter is an N wave. Their maximum overpressure is relatively small, about 1.5 Pa.

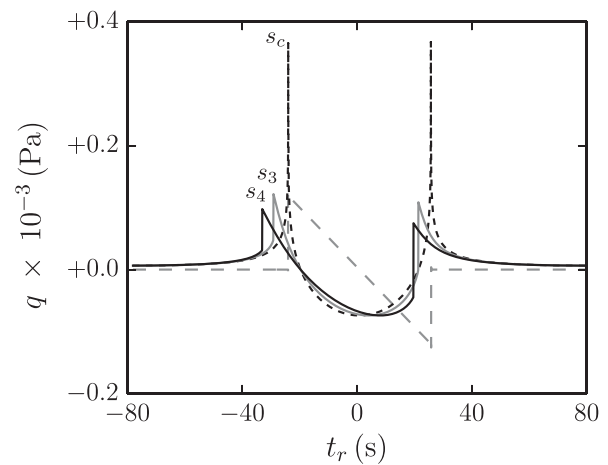
The evolution of the signature of the normalized pressure  $q$  along the lower thermospheric ray before the thermospheric caustic is plotted in Fig. 9(a). Because of non-linearities, the initial waveform evolves into an N-shaped wave, which lengthens while propagating toward the thermosphere. The duration  $T(s)$  is of about 4 s at  $s_1 = 44.2$  km, 22 s at  $s_2 = 175.5$  km and 50 s at  $s = s_c = 224$  km. Accordingly, the maximum of the pressure perturbation  $Q(s)$  diminishes approximately following the theoretical behaviour  $Q(s) \propto T^{-1}(s)$ , valid in the pure non-linear case (Pierce 1985).

The evolution of the signature of the normalized pressure  $q$  along the lower thermospheric ray after the thermospheric caustic is plotted in Fig. 9(b). As a consequence of the Hilbert transformation applied when the ray crosses the caustic, the initial waveform beyond the point  $s = s_c$  is a perfectly U-shaped wave. For  $s > s_c$ , two shocks are generated near the peaks and, as also highlighted by Rogers & Gardner (1980), the signal should again become an N wave. However, the roughly exponential increase of the density of the medium during the downward propagation beyond the caustic contributes to slow down the non-linear distortion. The waveform is found to be frozen for  $s \gtrsim s_l = 250$  km. This effect can be explained by examining the evolution of the function  $\tilde{x}(s)$ , as illustrated in Fig. 9(c). For  $s \gtrsim s_l$ , the increase of the distortion distance  $\tilde{x}(s)$  remains very small, no matter how far the wave propagates along the ray. Consequently, according to expression (15), no significant distortion can occur for  $s \gtrsim s_l$ . More generally, waveform freezing is likely to take place for any downward propagating phase. Hence, it can be deduced that the duration and the peak frequency of the signals detected at ground level mostly depends on the non-linear period lengthening during the upward propagation.

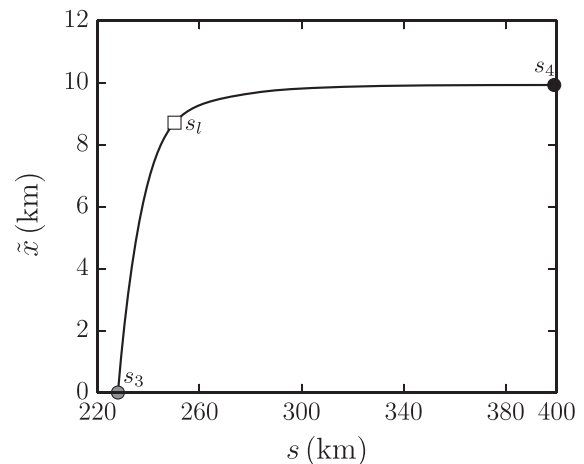
The pressure perturbation  $q$  computed on the upper thermospheric phase at  $s = 245.2$  km and the corresponding energy spectral density  $\mathcal{E}_q$  are plotted in Figs 10(a) and (b), respectively. Different regions can be identified in the spectrum. The function  $\mathcal{E}_q$  reaches its maximum value at  $f_p = 0.007$  Hz and about 93 per cent of the total energy of the signal is contained in the interval  $[0, 0.04]$  Hz. For frequencies  $f$  in the intermediate range  $[0.04, 0.4]$  Hz, dissipation is



(a)

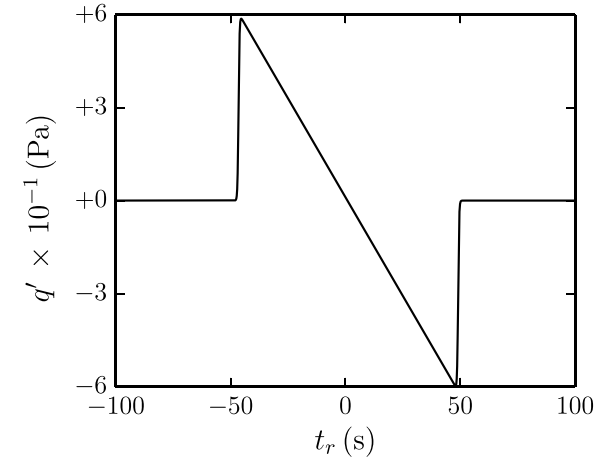


(b)

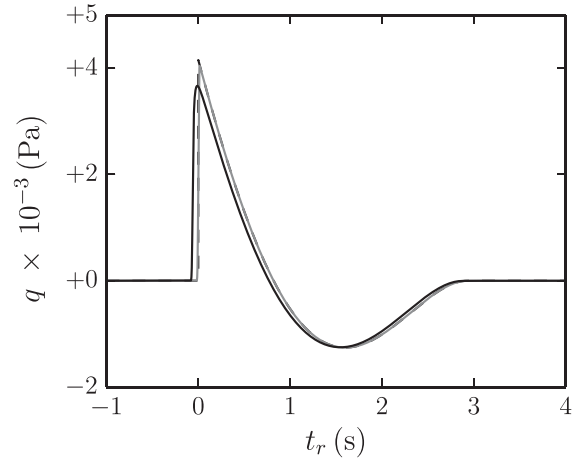


(c)

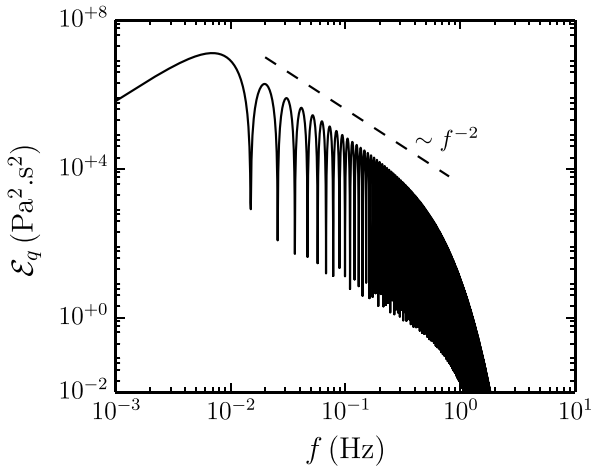
**Figure 9.** Results for case  $A$  on the lower thermospheric ray. (a) Signals  $q$  recorded at  $s_1 = 44.2$  km (dashed line),  $s_2 = 175.5$  km (grey line) and  $s_c$  before the caustic point. (b) Signals  $q$  recorded at  $s_c = 224$  km (black dashed line),  $s_3 = 228$  km (grey line) and  $s_4 = 399$  km (black line) after the caustic point. (c) Distortion distance  $\tilde{x}$  computed from  $s = s_3$  as a function of the curvilinear abscissa  $s$ .



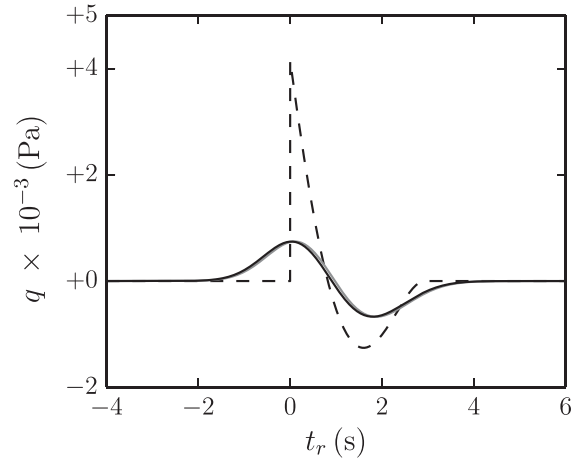
(a)



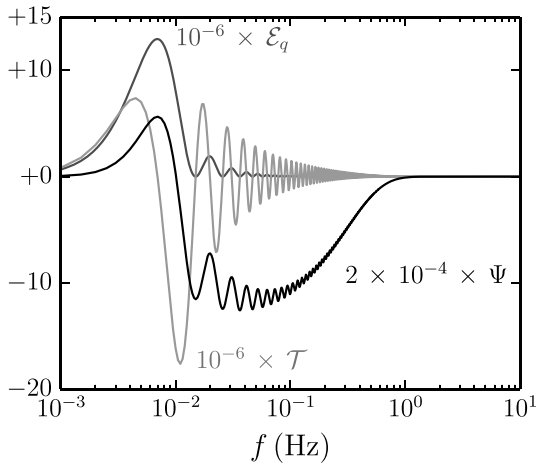
(a)



(b)



(b)



(c)

**Figure 10.** Case *A*. (a) Signal  $q$  obtained at  $s = 245.2$  km on the upper thermospheric ray and (b) corresponding energy spectral density  $\mathcal{E}_q$ . (c) Transfer term  $10^{-6} \times \mathcal{T}$  (light grey line), energy flux  $5 \times 10^{-3} \times \Psi$  from high to low frequencies (black line) and energy spectral density  $10^{-6} \times \mathcal{E}_q$  (grey line).

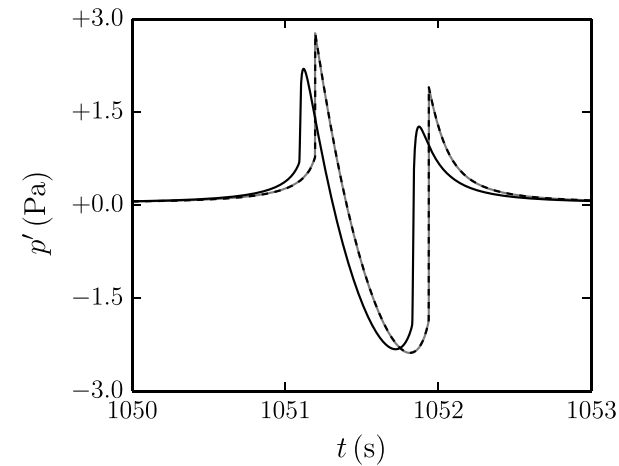
**Figure 11.** Case *A*. Signals  $q$  obtained at the caustic point on the (a) stratospheric and (b) lower thermospheric rays, with  $(S_{cl})$  (black line) and  $(S_{cl} + S_{vb})$  (grey line). The initial waveform is also reported (black dashed line).

negligible and the maxima of  $\mathcal{E}_q$  decrease as  $f^{-2}$ , as typically found for N waves (see Appendix B). Finally, for  $f > 0.4$  Hz, absorption becomes significant and the function  $\mathcal{E}_q$  drops with  $f$ . The term  $\mathcal{T}$  of eq. (19) computed for this signal is shown in Fig. 10(c). Since its sign oscillates with  $f$ , the non-linear transfer of energy seems to take place towards both higher and lower harmonics. More insights can be obtained by the analysis of the function  $\Psi(s, f)$  defined by

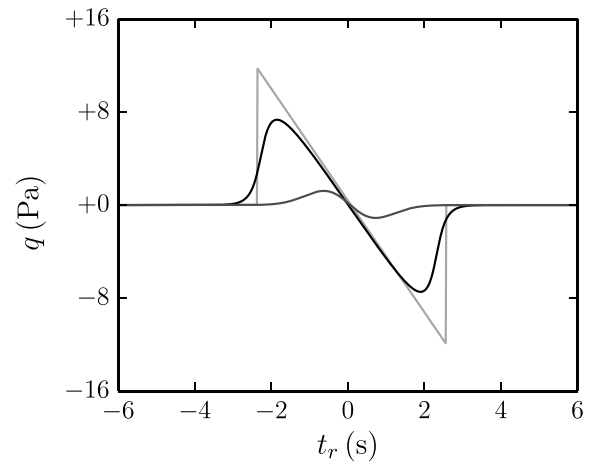
$$\Psi(s, f) = \int_0^f \mathcal{T}(s, \xi) d\xi \quad (42)$$

which represents the net energy transferred from spectral components of frequency greater than  $f$  to spectral components of frequency smaller than  $f$ . As a consequence of the low-frequency generation induced by the lengthening of the wave, the variable  $\Psi(s, f)$  reaches a local maximum around  $f = f_p$ . Nevertheless, beyond this point, the term  $\Psi(s, f)$  decreases and becomes negative, indicating that, despite the frequency shift, the energy is preferentially transferred towards higher harmonics.

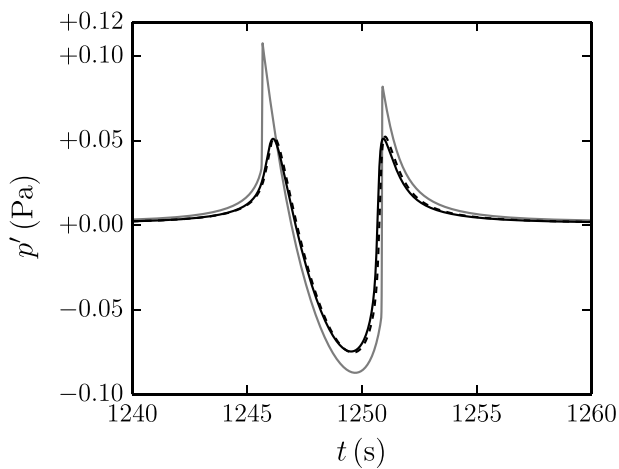
Signals obtained at the caustic points of the stratospheric and lower thermospheric paths in the linear propagation approximation are illustrated in Figs 11(a) and (b). On both rays, it is found that vibrational relaxation has a weak influence on the waveforms. The



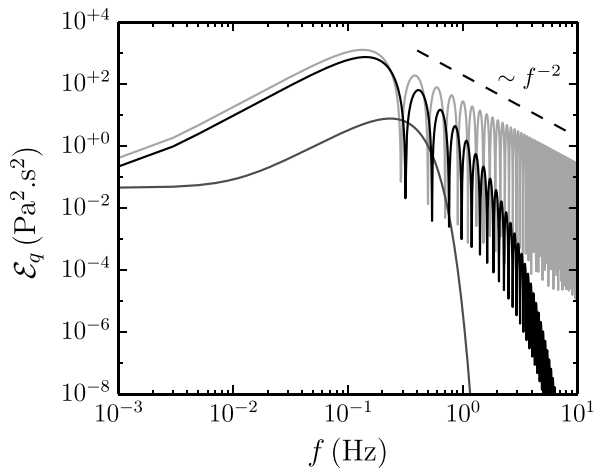
(a)



(a)



(b)



(b)

**Figure 12.** Case *B*. Stratospheric (a) and lower thermospheric (b) arrivals recorded at  $G_s$  with  $(S_{nl})$  (black dashed line),  $(S_{nl} + S_{cl})$  (grey line) and  $(S_{nl} + S_{cl} + S_{vb})$  (black line).

classical term play a minor role on the stratospheric trajectory, but induces a strong attenuation on the lower thermospheric path. On this ray, the amplitude of the phase  $I_{ta}$  at  $s = s_c$  is about 17.9 per cent of  $Q_0$  and its energy  $E(s_c)$  is around the 19.7 per cent of the initial value  $E(s_0)$ .

It is worth pointing out that, if the non-linear source term were also included, the ratio  $E(s_c)/E(s_0)$  would be about 0.048, four times smaller than in the linear case. This effect is a consequence of the aforementioned energy transfer towards higher harmonics, which are more attenuated than lower frequencies.

#### 4.5.2 Case *B*

The stratospheric and lower thermospheric arrivals recorded at  $G_s$  are plotted in Figs 12(a) and (b), respectively. The former has a duration of about 1 s and a maximum of overpressure of the order of 1 Pa. The latter has a higher period, but its amplitude is more than 10 times smaller. Concerning the stratospheric arrival, results obtained in the pure non-linear case (only with the source term  $S_{nl}$ ) and with the source term  $(S_{nl} + S_{cl})$  are nearly superimposed, indicating that classical absorption effects play a minor role on the wave-

**Figure 13.** Case *B*. (a) Signals  $q$  recorded at the caustic point on the lower thermospheric ray with  $(S_{nl})$  (black dashed line),  $(S_{nl} + S_{cl} + S_{vb})$  (grey line) and  $(S_{cl} + S_{vb})$  (black line). (b) Corresponding energy spectral densities  $E_q$ .

form. On the contrary, vibrational relaxation induces a reduction of about 20 per cent on the maximum of overpressure. Dispersion is also visible on the stratospheric phase. The lag is however very small if compared to the time arrival of the signal. Different trends are observed on the lower thermospheric ray, where classical absorption is the major dissipation mechanism, whereas vibrational relaxation does not affect the recorded signal. The maximum of the pressure perturbation is almost halved with respect to the inviscid non-relaxing case.

The interaction between non-linear and absorption effects is emphasized in Fig. 13(a) which illustrates the signals  $q$  recorded at the caustic point of the lower thermospheric ray with the source terms  $S_{nl}$  and  $(S_{nl} + S_{cl} + S_{vb})$ . The corresponding energy spectral densities  $E_q$  are plotted in Fig. 13(b). No intermediate range is found for the present case, and dissipation, which is mainly due to the classical mechanisms, affects also the energy-containing spectral components. As a result, the amplitude observed with all source terms is reduced by a factor of 1.6 with respect to that obtained in the pure non-linear case. The duration of the phase, which depends on the non-linear lengthening, is also slightly decreased. The signal  $q$  obtained with the source term  $S_{cl} + S_{cl}$  is reported in Fig. 13(a) as

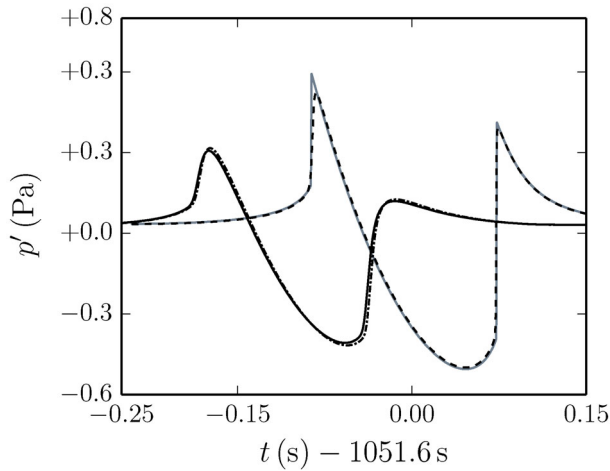


**Figure 14.** Case C. Stratospheric arrival recorded at  $G_s$  with  $(S_{nl})$  (black dashed line),  $(S_{nl} + S_{cl})$  (grey line) and  $(S_{nl} + S_{cl} + S_{vb})$  (black line). The solution obtained in the full model case but only with the vibrational relaxation of oxygen and nitrogen considered is plotted in black dash-dotted line.

well, in order to highlight the importance of non-linearity. For the present source yield, the non-linear shift toward lower frequencies strongly attenuates the impact of absorption. If  $S_{nl}$  were set to zero, the amplitude would be six times lower if compared to the solution of the complete configuration, and the duration would be almost halved.

#### 4.5.3 Case C

The stratospheric arrival recorded at  $G_s$  is plotted in Fig. 14. The results obtained only with the non-linear term  $(S_{nl})$  and with also classical absorption included  $(S_{nl} + S_{cl})$  are nearly superimposed. On the contrary, vibrational relaxation has a strong impact on the maximum amplitude. The signal recorded by considering only the oxygen  $O_2$  and nitrogen  $N_2$  terms is also reported in Fig. 14. As expected, the deviation from the full model case is weak, demonstrating that, for the range of frequencies under study, vibrational relaxation of oxygen  $O_2$  and nitrogen  $N_2$  constitute the most important contribution to the absorption along stratospheric paths.

## 5 CONCLUSIONS

Using non-linear ray theory, the propagation in a realistic atmosphere of signals induced by explosive phenomena and of main frequencies between about 0.1 and 15 Hz is investigated in order to assess the importance of absorption and non-linear effects on the waveforms recorded at ground level, at distances of a few hundreds kilometres. Three cases with different source amplitudes, corresponding to waves generated by phenomena ranging from small volcanic eruptions to large chemical explosions, are examined, and the results obtained on stratospheric and thermospheric rays are discussed. For high-amplitude and low-frequency signals, the propagation is found to be essentially non-linear. The influence of the dissipation terms on the signature obtained at ground level increases with increasing frequency and decreasing amplitude. In the infrasound range, attenuation is induced by vibrational relaxation on stratospheric rays, whereas the classical mechanisms become dominant on thermospheric rays, mainly because of the roughly exponential decrease of the density with altitude. The most impor-

tant contribution to relaxation absorption below the stratospheric limit is given by the vibrational modes of oxygen and nitrogen, at least for the frequencies under study. Nonetheless, the relaxation processes of carbon dioxide and ozone may affect thermospheric phases while travelling across the mesosphere. Dispersion induced by vibrational relaxation is also observed on the simulated signals, but the effect is negligible. Overall, relaxation absorption should be taken into account on stratospheric rays for frequencies higher than about 1 Hz, whereas classical absorption may be important on thermospheric rays also for lower frequencies.

The interaction between absorption and non-linear terms is also revisited on thermospheric rays. For large amplitude and low-frequency explosions, the classical absorption and vibrational relaxation terms, although responsible for energy depletion, have weak influence on the waveform, as they act only near shock fronts. For smaller explosions with higher frequency content, the dissipation terms may also affect the energy-containing spectral components of the wave, inducing an important reduction of its amplitude and limiting the non-linear lengthening. On the other hand, the impact of non-linearity is also likely to be significant, as the non-linear shift toward lower frequencies prevents the strong attenuation predicted by linear theory.

In the cases examined in this work, waveform freezing is observed as well. The duration of the signal recorded at ground level mainly depends on its lengthening during the propagation towards the upper atmosphere and around the caustic. Beyond this point, distortion is considerably slowed down by the roughly exponential increase of the atmospheric density and the propagation towards the Earth's surface can be considered linear.

## ACKNOWLEDGEMENTS

Present results have been obtained within the framework of LETMA (Laboratoire Études et Modélisation Acoustique), a Contractual Research Laboratory shared between CEA, CNRS, École Centrale de Lyon, C-Innov and Université Pierre et Marie Curie. This work was granted access to the HPC resources of the Très Grand Centre de calcul du CEA (TGCC) under the allocation 2015-200204 made by GENCI (Grand Equipement National de Calcul Intensif). Authors express gratitude to the Direction Générale de l'Armement (DGA) for the financial support.

## REFERENCES

- Bailly, C. & Comte-Bellot, G., 2015. The dynamics of isotropic turbulence, in *Turbulence*, Chap. 7, pp. 186–188, Springer, Cham.
- Bass, H.E., Hetzer, C.H. & Raspet, R., 2007. On the speed of sound in the atmosphere as a function of altitude and frequency. *J. geophys. Res.*, **112**, D15110, doi:10.1029/2006JD007806.
- Berland, J., Bogey, C. & Bailly, C., 2006. Low-dissipation and low-dispersion fourth-order Runge–Kutta algorithm, *Comp. Fluids*, **35**, 1459–1463.
- Bogey, C. & Bailly, C., 2004. A family of low dispersive and low dissipative explicit schemes for noise computations, *J. Comput. Phys.*, **194**(1), 194–214.
- Bogey, C., De Cacqueray, N. & Bailly, C., 2009. A shock-capturing methodology based on adaptive spatial filtering for high-order nonlinear computations, *J. Comput. Phys.*, **228**, 1447–1465.
- Brachet, N., Brown, D., Le Bras, R., Cansi, Y., Mialle, P. & Coyne, J., 2010. Monitoring the Earth's atmosphere with the global IMS infrasound network, in *Infrasound Monitoring for Atmospheric Studies*, Chap. 3, pp. 77–118, Springer, Dordrecht.

- Campus, P. & Christie, D.R., 2010. Worldwide observations of infrasonic waves, in *Infrasound Monitoring for Atmospheric Studies*, Chap. 6, pp. 185–234, Springer, Dordrecht.
- Candel, S.M., 1977. Numerical solution of conservation equations arising in linear wave theory: application to aeroacoustics, *J. Fluid Mech.*, **83**(3), 465–493.
- Christie, D.R. & Campus, P., 2010. The IMS infrasound network: design and establishment of infrasound stations, in *Infrasound Monitoring for Atmospheric Studies*, Chap. 2, pp. 29–75, Springer, Dordrecht.
- Cleveland, R.O., 1995. Propagation of sonic booms through a real, stratified atmosphere, *PhD thesis*, The University of Texas at Austin.
- Cleveland, R.O., Hamilton, M.F. & Blackstock, D.T., 1996. Time-domain modeling of finite-amplitude sound in relaxing fluids, *J. acoust. Soc. Am.*, **99**(6), 3312–3318.
- de Groot-Hedlin, C., 2008. Finite-difference time-domain synthesis of infrasound propagation through an absorbing atmosphere, *J. acoust. Soc. Am.*, **124**(3), 1430–1441.
- de Groot-Hedlin, C., Hedlin, M.A.H. & Walker, K., 2011. Finite difference synthesis of infrasound propagation through a windy, viscous atmosphere: application to a bolide explosion detected by seismic networks, *Geophys. J. Int.*, **185**(1), 305–320.
- de Groot-Hedlin, C., 2012. Nonlinear synthesis of infrasound propagation through an inhomogeneous, absorbing atmosphere, *J. acoust. Soc. Am.*, **132**(2), 646–656.
- de Groot-Hedlin, C., 2016. Long-range propagation of nonlinear infrasound waves through an absorbing atmosphere, *J. acoust. Soc. Am.*, **139**(4), 1565–1577.
- Fee, D. et al., 2013. Overview of the 2009 and 2011 Sayarim infrasound calibration experiments, *J. geophys. Res.*, **118**(12), 6122–6143.
- Gainville, O., Piserchia, P.F., Blanc-Benon, P. & Scott, J., 2006. Ray tracing for long range atmospheric propagation of infrasound, in *12th AIAA/CEAS Aeroacoustics Conference*, pp. 1–17, 2006 May 8–10, Cambridge, MA.
- Gainville, O., 2008. Modélisation de la propagation atmosphérique des ondes infrasonores par une méthode de tracé de rayons non linéaire (Numerical modelling of atmospheric infrasound propagation using a nonlinear ray-tracing method), *PhD thesis*, Ecole Centrale de Lyon, No. 2008-07.
- Gainville, O., Blanc-Benon, P., Blanc, E., Roche, R., Millet, C., Le Piver, F., Despres, B. & Piserchia, P.F., 2010. Misty picture: a unique experiment for the interpretation of the infrasound propagation from large explosive sources, in *Infrasound Monitoring for Atmospheric Studies*, Chap. 18, pp. 575–598, Springer, Dordrecht.
- Hamilton, M.F. & Blackstock, D.T., 2008. *Nonlinear Acoustics*, Acoustical Society of America.
- Hanique-Cockenpot, G., Bailly, C., Bogey, C. & Marsden, O., 2010. Intégration de la relaxation dans les équations de Navier-Stokes pour la propagation sonore, in *10ème Congrès Français d'Acoustique*, April 2010, Lyon, France.
- Kinney, G.F. & Graham, K.J., 1985. *Explosive Shocks in Air*, Springer-Verlag, Berlin Heidelberg.
- Kravtsov, Yu.A. & Orlov, Yu.I., 1993. *Caustics, Catastrophes and Wave Fields*, Springer-Verlag.
- Lonzaga, J.B., Waxler, R.M., Assink, J.D. & Talmadge, C.L., 2015. Modelling waveforms of infrasound arrivals from impulsive sources using weakly nonlinear ray theory, *Geophys. J. Int.*, **200**(3), 1347–1361.
- Marsden, O., Bailly, C. & Bogey, C., 2014. A study of infrasound propagation based on high-order finite difference solutions of the Navier–Stokes equations, *J. acoust. Soc. Am.*, **135**(3), 1083–1095.
- Mutschlecner, J.P. & Whitaker, R.W., 2010. Some atmospheric effects on infrasound signal amplitudes, in *Infrasound Monitoring for Atmospheric Studies*, Chap. 14, pp. 455–474, Springer, Dordrecht.
- Ottmoller, L. & Evers, L.G., 2007. Seismo-acoustic analysis of the Buncefield oil depot explosion in the UK, 2005 December 11, *Geophys. J. Int.*, **172**, 1123–1134.
- Pierce, A.D., 1978. Aeroacoustic fluid dynamic equations and their acoustic energy conservation corollary with O<sub>2</sub> and N<sub>2</sub> vibrational relaxation effects included, *J. Sound Vib.*, **58**(2), 189–200.
- Pierce, A.D., 1985. *Acoustics: An Introduction to Its Physical Principles and Applications*, Acoustical Society of America.
- Rallabhandi, S.K., 2011. Advanced sonic boom prediction using augmented Burgers' equation, in *49th AIAA Aerospace Sciences Meeting*, pp. 1–17, 2011 January 4–7, Orlando, Florida.
- Rayleigh, J.W.S., 1878. *The Theory of Sound*, Vol. II, Dover Publications, New York (2nd edn published in 1945).
- Reed, J.W., 1977. Atmospheric attenuation of explosion waves, *J. acoust. Soc. Am.*, **61**(1), 39–47.
- Ripepe, M. & Marchetti, E., 2002. Array tracking of infrasonic sources at Stromboli volcano, *Geophys. Res. Lett.*, **29**(22), 2076, doi:10.1029/2002GL015452.
- Rogers, P.H. & Gardner, J.H., 1980. Propagation of sonic booms in the thermosphere, *J. acoust. Soc. Am.*, **67**(1), 78–91.
- Sabatini, R., Marsden, O., Bailly, C. & Gainville, O., 2015. Numerical simulation of infrasound propagation in the Earth's atmosphere: study of a stratospherical arrival pair, in *AIP Conf. Proc.*, **1685**, 090002; 29 June–3 July 2015, Écully, France.
- Sabatini, R., Marsden, O., Bailly, C. & Bogey, B., 2016. A numerical study of nonlinear infrasound propagation in a windy atmosphere, *J. acoust. Soc. Am.*, **140**(1), 641–656.
- Sutherland, L.C. & Bass, H.E., 2004. Atmospheric absorption in the atmosphere up to 160 km, *J. acoust. Soc. Am.*, **115**(3), 1012–1032. [See also Erratum *J. acoust. Soc. Am.*, **120**(5), 2985 (2006).]
- Wochner, M.S., Atchley, A.A. & Sparrow, V.W., 2005. Numerical simulation of finite amplitude wave propagation in air using a real-alistic atmospheric absorption model, *J. acoust. Soc. Am.*, **118**(5), 2891–2898.
- Yamamoto, M., Hashimoto, A., Aoyama, T. & Sakai, T., 2015. A unified approach to an augmented Burgers' equation for the propagation of sonic booms, *J. acoust. Soc. Am.*, **137**(4), 1857–1866.

## APPENDIX A: EQUATION GOVERNING THE ENERGY SPECTRAL DENSITY

The augmented Burgers equation (9) can be rewritten in the spectral domain as

$$\frac{\partial \hat{q}}{\partial s} = + \frac{i \pi f \beta_e}{\bar{\rho}_0 \bar{c}_0^3} \hat{\varepsilon} - \alpha \hat{q} - i d_{vb} \hat{q} \quad (\text{A1})$$

where  $\hat{\varepsilon}$  is the Fourier transform of the variable  $q^2$

$$\hat{\varepsilon}(s, f) = \int_{-\infty}^{+\infty} q^2(s, t_r) e^{-i2\pi f t_r} dt_r \quad (\text{A2})$$

and the real coefficient  $d_{vb}$  represents the dispersion effect induced by the vibrational relaxation term. Taking the complex conjugate of eq. (A1) yields

$$\frac{\partial \hat{q}^*}{\partial s} = - \frac{i \pi f \beta_e}{\bar{\rho}_0 \bar{c}_0^3} \hat{\varepsilon}^* - \alpha \hat{q}^* + i d_{vb} \hat{q}^* \quad (\text{A3})$$

By multiplying eq. (A1) by  $\hat{q}^*$  and eq. (A3) by  $\hat{q}$ , by adding these relations and by multiplying the result by a factor 2, the Lin's equation (19) is obtained for the one-sided spectrum  $\mathcal{E}_q$

$$\frac{\partial \mathcal{E}_q}{\partial s} = \frac{\beta_e}{\bar{\rho}_0 \bar{c}_0^3} \mathcal{T} + \mathcal{D} \quad (\text{A4})$$

The non-linear transfer and dissipation terms are, respectively, given by

$$\begin{aligned} \mathcal{T}(s, f) &= i2\pi f [\hat{q}^*(s, f) \hat{\varepsilon}(s, f) - \hat{q}(s, f) \hat{\varepsilon}^*(s, f)] \\ \mathcal{D}(s, f) &= -2\alpha(s, f) \mathcal{E}_q(s, f). \end{aligned} \quad (\text{A5})$$

By using the properties of the convolution product and recalling that the Fourier transform of a real function is Hermitian, the term

$\hat{\varepsilon}$  can be further developed as

$$\hat{\varepsilon}(s, f) = \int_0^f \hat{q}(s, \zeta) \hat{q}(s, f - \zeta) d\zeta + 2 \int_f^{+\infty} \hat{q}(s, \zeta) \hat{q}^*(s, \zeta - f) d\zeta \quad (\text{A6})$$

which shows that the non-linear transfer term  $\mathcal{T}$  is responsible for the interaction of the spectral component of frequency  $f$  with lower and higher harmonics.

Integrating eq. (A4) over all frequencies yields

$$\frac{dE}{ds} = \frac{\beta_e}{\bar{\rho}_0 \bar{c}_0^3} \int_0^{+\infty} \mathcal{T} df + \int_0^{+\infty} \mathcal{D} df. \quad (\text{A7})$$

Eq. (A7) can also be derived by multiplying eq. (9) by  $q$  and by integrating over time. It can be shown that

$$\frac{dE}{ds} = \frac{\beta_e}{\bar{\rho}_0 \bar{c}_0^3} \int_{-\infty}^{+\infty} q \frac{\partial q^2}{\partial t_r} dt_r + \int_{-\infty}^{+\infty} 2q(S_{cl} + S_{vb}) dt_r. \quad (\text{A8})$$

Consequently, by comparison between eqs (A7) and (A8), it may be deduced that

$$\int_0^{+\infty} \mathcal{T} df = \int_{-\infty}^{+\infty} q \frac{\partial q^2}{\partial t_r} dt_r = \frac{2q^3}{3} \Big|_{-\infty}^{+\infty} = 0 \quad (\text{A9})$$

since the signal  $q$  vanishes as  $t_r$  goes to  $\pm\infty$ .

## APPENDIX B: SPECTRUM OF AN N WAVE

The one-sided spectrum  $\mathcal{E}_q = 2|\hat{q}|^2$  of an N wave of the form

$$q(t_r) = \begin{cases} -\frac{Q}{T} t_r & t_r \in ]-T, +T[ \\ 0 & \text{otherwise} \end{cases} \quad (\text{B1})$$

is given by

$$\mathcal{E}_q = \frac{2Q^2}{T^2} \left[ \frac{T \cos(2\pi f T)}{\pi f} - \frac{\sin(2\pi f T)}{\pi^2 f^2} \right]^2 \quad (\text{B2})$$

and its maxima decrease as  $f^{-2}$  when the frequency  $f$  goes to  $+\infty$ .